MHD Simulation of High Wavenumber Ballooning-like Modes in LHD

H. Miura and N. Nakajima

National Institute for Fusion Science, 322-6 Oroshi, Toki, Gifu 509-5292, JAPAN

e-mail contact of main author:miura.hideaki@nifs.ac.jp

Abstract. Dynamical growths of high-wavenumber ballooning modes are studied through full-3D nonlinear MHD simulations of the Large Helical Device. The growths of the ballooning modes are identified by studying the growth rates and the radial profiles of the Fourier coefficients of fluctuation variables. The mechanisms to weaken the growth of instability, such as the local fattening of the pressure and the energy release to the parallel kinetic energy, are found being insufficient to suppress the high-wavenumber ballooning modes. Consequently, the mean pressure profile is totally modified when the evolutions of the ballooning modes are saturated. The numerical results reveal that we need some mechanisms which do not originate from an ideal MHD to achieve a mild, saturated behaviors beyond the growths of unstable high ballooning modes in the helical device. The parallel heat conductivity is proposed as one of possible non-ideal mechanisms.

1 Introduction

Magnetohydrodynamic (MHD) stability is one of the key issues of plasma dynamics in magnetic confinement devices such as the Large Helical Device (LHD)[1] as well as other type of devices. The LHD is a heliotron/torsatron type helical device with a set of L=2/M=10 helical coils with the major radius 3.9m [1]. Linear stability analyses of the LHD predict short-wave instabilities such as the interchange and/or ballooning instabilities, especially for the position of the magnetic axis $R_{ax} < 3.75m$ (*inward-shifted configuration*). However, in spite of the unstable predictions, high β values of about 5% have been achieved in the LHD experiments under the inward-shifted magnetic configurations (typically $R_{ax} = 3.6m$)[2]. In the experiments, some signals with low poloidal(m) and toroidal (n) modes are identified as MHD activities but the activities do not bring about crash of the pressure profiles.[3, 4]

Aiming to clarify mechanisms of a hot plasma to overcome the predicted instabilities, some numerical works including fully three-dimensional (3D) MHD direct numerical simulations[5, 6, 7], reduced MHD simulations[9] and the compressible linear stability analysis[10] have been carried out. Some possible mechanisms to weaken the instabilities are proposed through these numerical works: the local pressure flattening, the release of the free energy as the flows parallel to the magnetic field, and the compressibility effect to reduce the linear growth rates. While these numerical researches have been conducted carefully, influences of the growths of high-wavenumber unstable linear eigen-modes, or high modes, over the low modes in the interchange/ballooning instability remain unclear. Here we use the word *high* meaning roughly $n \simeq M$ or higher. The study of the growths of high modes can be essential among many theoretical subjects. In numerical simulations focusing on dynamics of low modes, there appears an implicit expectation that the high modes are suppressed or saturated by the local flattening of the pressure or some other mechanisms, and stay harmless for the global dynamics of helical plasmas. The hypothesis should be examined to make the numerical works be conclusive. The verification may also contribute to help theoretical understandings of data in real experiments, in which it is difficult to identify high modes. The main

subject of this paper is to carry out simulations which achieve growths of high modes and study influences of high modes over low modes.

This paper is organized as follows. In the next section, outlines of our numerical simulations are introduced. Growths of high-wavenumber ballooning modes are studied by means of full-3D MHD simulations in §.3. A possible milder saturations of the ballooning modes by the introduction of the parallel heat conductivity is studied in §.4. Summary is in the last section.

2 Outlines of numerical simulations

We carry out numerical simulations by the use of the MHD In Non-Orthogonal System (MINOS) code[6, 8]. In the MINOS code, the 3D compressible and nonlinear MHD equations are expressed in terms of the contravariant coefficients in the helical-toroidal coordinate system (u^1, u^2, u^3). The spatial derivatives are approximated by the 8th order compact finite difference scheme[11]. The Runge-Kutta-Gill scheme of the 4th order accuracy is adopted for the marching in the time-direction. The number of grid points is $N_S = 193 \times 193 \times 640$. Simulations with a larger number of grid points $N_L = 385 \times 385 \times 640$ are also carried out for short periods to check the numerical convergence. A difference of simulations in this article from the earlier works [5, 6, 7, 8] is that a hyper viscosity of $\partial^4/\partial u_i^4$ is implemented to avoid a numerical explosion in a low-viscosity simulation in this article. The influences of the hyper viscosity will be seen later. We also note introducing the Boozer coordinate (ψ, θ, ζ) where ψ, θ and ζ are the normalized toroidal flux, the poloidal and the toroidal angles, respectively, for the purpose of studying the linear instability in the simulations. Fourier coefficients of a quantity A are computed in the Boozer coordinate system as

$$\begin{aligned} A_{mn}(\psi) &= \oint d\theta \oint d\zeta A(\psi,\theta,\zeta)\exp[i(m\theta - n\zeta)] \\ &= \oint d\theta \oint d\zeta A(u^1(\psi,\theta,\zeta), u^2(\psi,\theta,\zeta), u^3(\psi,\theta,\zeta))\exp[i(m\theta - n\zeta)]. \end{aligned} \quad (1)$$

A 3D vector is decomposed into the three orthogonal components, $\boldsymbol{e}_{\nabla\psi} = \nabla\psi/|\nabla\psi|$, $\boldsymbol{e}_b = \boldsymbol{B}/|\boldsymbol{B}|$, $\boldsymbol{e}_{\nabla\psi\times b} = \boldsymbol{e}_{\nabla\psi} \times \boldsymbol{e}_b$, as $\boldsymbol{V} = V^{\nabla\psi}\boldsymbol{e}_{\nabla\psi} + V^b\boldsymbol{e}_b + V^{\nabla\psi\times b}\boldsymbol{e}_{\nabla\psi\times b}$ where $\boldsymbol{B}$ is the magnetic field vector and the three components are Fourier transformed. See Ref.[6] for details.

Numerical simulations are carried out for the inward-shifted magnetic configuration with $R_{ax} = 3.6m$. The initial condition of the MHD equations is composed of the net toroidal current free MHD equilibrium, which is provided by the HINT computation[12], and perturbations to the equilibrium which are given as the trigonometric functions with random amplitudes and phases in the (u^1, u^2, u^3)-coordinate system. The initial pressure has a peaked profile $p(\psi_0) = P_0(1-\psi_0^2)$ where the ψ_0 is the initial toroidal magnetic flux (the initial poloidal flux ψ_0 is slightly different from the toroidal flux ψ of the Boozer coordinate) and the peak beta value $\beta \equiv P_0/(B_0^2/2)$ is 3.7% . The averaged beta value is $\langle\beta\rangle \sim 1.2\%$ where $\langle\ \rangle$ is the volume average over the finite β region. In Fig.1, the mean pressure P_{00} (the $m/n = 0/0$ Fourier coefficient of the pressure) normalized by the magnetic pressure $B_0^2/2$ at the magnetic axis, the rotational transform $\iota/2\pi$ and D_I with positive value (multiplied by $1/20$) are plotted as the function of the normalized minor radius defined as $\sqrt{\psi}$. The D_I plot indicates that pressure-driven modes with their rational surfaces at $\sqrt{\psi} < 0.6$ ($\sqrt{\psi} > 0.6$) are linearly unstable (stable).

In the MINOS code, we have dissipative coefficients being normalized by some representative

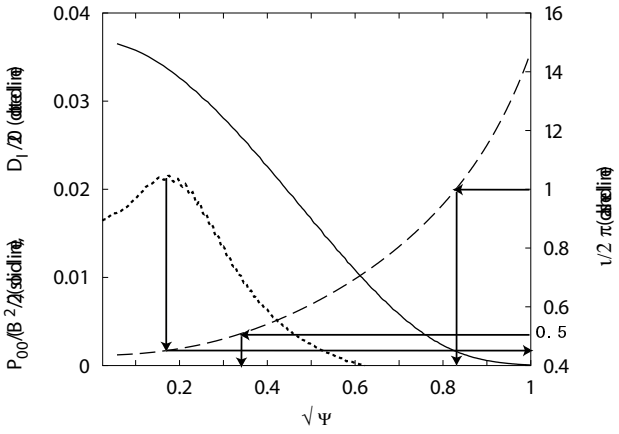

FIG. 1: Radial pressure profile of the initial equilibrium. The radial profile of the P_{00}, $\iota/2\pi$ and the stabilizing parameter D_I of the initial equilibrium are plotted. Solid arrows are drawn to indicate position of some typical rational surfaces and/or ι-values.

quantities: the resistivity η, viscosity μ, the isotropic portion of the heat conductivity κ and the parallel heat conductivity $\kappa_{\|}$. Simulations in this article are performed for two sets of parameters. The first one is for a near-ideal simulation: $\eta = \mu = \kappa = 1 \times 10^{-6}$ and $\kappa_{\|} = 0$. The other one is for studying a growth with a parallel heat conductivity: $\eta = \mu = \kappa = 1 \times 10^{-6}$ and $\kappa_{\|} = 10^{-2}$. Hereafter we focus on simulations with the former parameters ($\kappa_{\|} = 0$) and the simulation with $\kappa_{\|} = 10^{-2}$ is studied in §.4 only for the comparisons with the former one. We emphasize that the viscosity $\mu = 1 \times 10^{-6}$ is quite smaller than that in our earlier simulations[5, 6, 7, 8]. It enables near-ideal growths of unstable modes and it is the reason we need to introduce the hyper viscosity.

3 Growth of high-wavenumber Ballooning modes

In Fig.2(a), the total amplitudes of the three components of the velocity vector, $(V^i)^2 = \sum_{m,n} {V^i_{mn}}^2$ ($i = \nabla\psi, b, \nabla\psi \times b$) are shown. The three components experience the exponential growths during $40\tau_A \leq t \leq 70\tau_A$, where τ_A is the toroidal Alfvén time unit. Hereafter, we assume this Alfvén time unit and omit the symbol from the text. The instability which govern the exponential growths is identified later. The parallel energy $\left(V^b\right)^2$ is about 10 times as large as the normal energy $\left(V^{\nabla\psi}\right)^2$ and the binormal energy $\left(V^{\nabla\psi\times b}\right)^2$ at the saturate time $t \simeq 120$. The superiority of the parallel component over the other two components after the saturations has been observed in more viscous simulations[6, 7] too. The time evolutions of the typical Fourier amplitudes of the perpendicular (normal and binormal) and the parallel components of the velocity vector are shown in Fig.2(b) and (b), respectively. The representative wavenumbers plotted in Fig.2(b) and (c) are chosen so that they have resonant rational surfaces initially and attain large amplitudes, with the help of the study on the power spectra of the pressure which is shown later. When the time evolutions are saturated, the Fourier coefficients with low *n*s retain large amplitudes while the high-*n* coefficients become less energetic. It is especially clear in Fig.2(c). The high-*n* coefficients loose their amplitudes quickly at $t \simeq 90$. The decrease occurs in very short periods so that it should be attributed to the nonlinear scatterings of the energy into the wide range of the wavenumber space rather than to the viscous dissipations. On the other hand, the $m/n = 2/1$ coefficient keeps its energy and remain as the only-one dominant Fourier coefficient after the saturation. The dominance of low-*n* coefficients due to nonlinear couplings may make a sense to validate focusing on dynamics of low modes in numerical simulations of helical plasmas. In Fig.2(d), the growth rates of the Fourier coefficients in Fig.2(b) (and (c) as well) are compared to those of the ideal and linear MHD system obtained by the use of the CAS3D code[13]. The two groups of growth rates coincide with each other well. It shows that the growths of Fourier coefficients in the simulation are *near-ideal* and suitable to

study influences of unstable high modes.

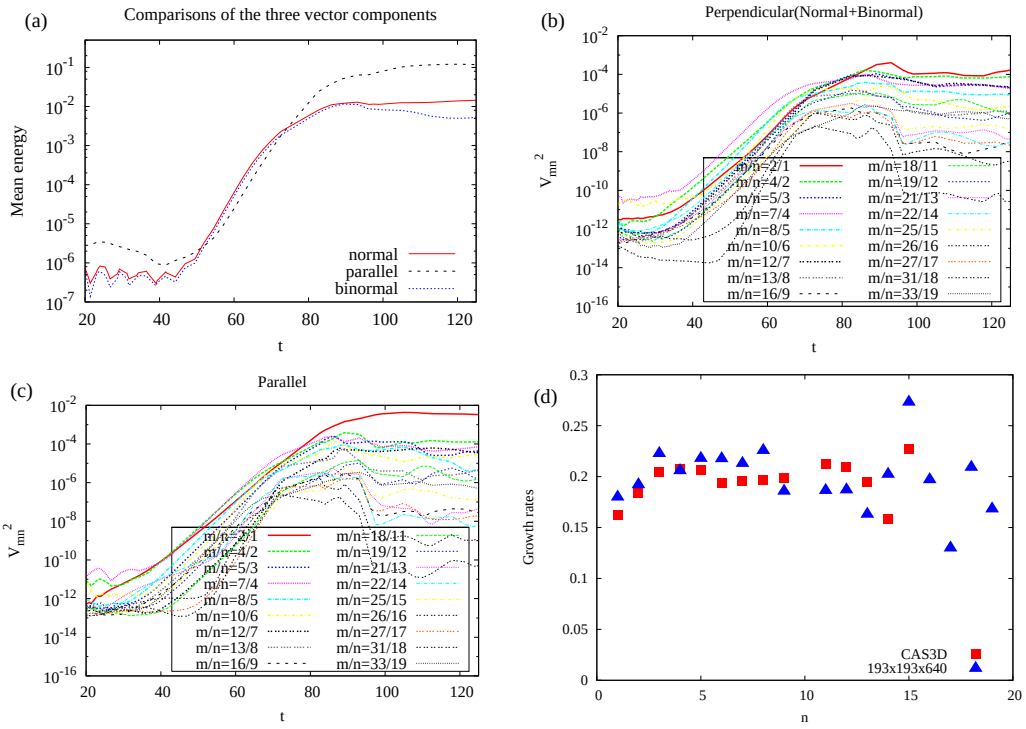

FIG. 2: (a)The time evolutions of $V^2 = \sum_{m,n} {V^i_{mn}}^2$ ($i = \nabla\psi, b, \nabla\psi \times b$). The amplitudes of ${V^i_{mn}}^2$ with some typical m/n-s for (b)the perpendicular (sum of the normal and binormal), and (c)the parallel components. (d)The growth rates of the Fourier amplitudes.

Here we note on numerical convergences. We have compared the growth rates in the simulations without the hyper viscosity between the simulations with numbers of grid points N_S and N_L. It can be shown by the comparison that the numerical convergence is fine for the exponential growths. Next, the growth rates have been compared between the simulations of the number of grid points N_S with and without the hyper viscosity. The agreement is well for $n < 20$, the deviations of growth rates being comparable with those in Fig.2(d). Finally, the influences of the hyper viscosity on each of m/n Fourier coefficients have been examined by controlling its strength. It is found that growth of some Fourier coefficients can be decelerated especially for $m > 20$ (the deceleration becomes clearer for larger m) and the influences of the decelerations can be important in the saturation processes of the time evolutions. Due to the influences, we refrain from discussing on the detailed dynamics in nonlinear processes and focus on qualitative views on the saturation processes.

The instability which governs the exponential growths in Fig.2 is identified to understand the dynamics of the helical plasma. The Fourier coefficients of the fluctuation variables are classified by their growth rates, since the Fourier coefficients which compose the same linear eigen-function must grow in the same growth rates except the influences of the viscosity. In Fig.3, radial profiles of the pressure Fourier coefficients which are considered to form one linear eigen-function are plotted for (a)$n = 1$, (b)8, (c)9 and (d)11 at $t = 60$. For simplicity, either the cosine or the sine part of the Fourier coefficients, P^C_{mn} or P^S_{mn} respectively, are plotted. Some Fourier coefficients, $n = 9$ coefficients in for the $n = 1$ mode for example, are also omitted from the figures for the simplicity, too. In Fig.3(a), $P^S_{m,n=1}$ for $1 \le m \le 4$ are shown. The primary Fourier coefficient of the $n = 1$, $P_{2,1}$ has a broad peak from $\sqrt{\psi} = 0.3$ to 0.4. (The $\iota/2\pi = 0.5$ rational surface is at $\sqrt{\psi} \simeq 0.35$.)

As n goes higher, the widths of the radial profiles of the primary coefficients becomes narrower. A common feature in Fig.3(a)-(d) is that the most dominant Fourier coefficients, (a)$m/n = 2/1$, (b)$13/8$, (c)$16/9$ and (d)$18/11$ have no zero in the radial direction. It exhibits a typical characteristics of a primary coefficient of a linear eigen-function. We find a larger number of the Fourier coefficients (subsidal coefficients) which grow with the primary coefficients for larger n. These subsidal Fourier coefficients have also finite amplitudes, showing that the linear eigen-function for each n should be composed of multiple Fourier coefficients for a wide range of the wavenumber (a broad-band property).

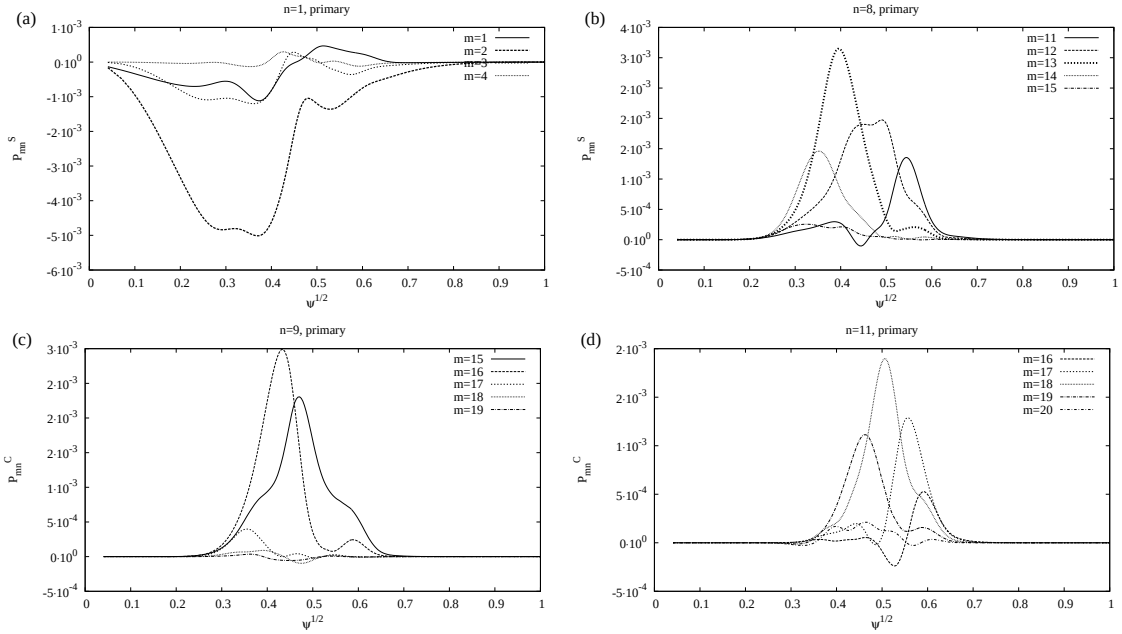

FIG. 3: The radial profiles of the pressure Fourier coefficients of (a)$n = 1$, (b)$n = 8$, (c)$n = 9$ and (d)$n = 11$ modes.

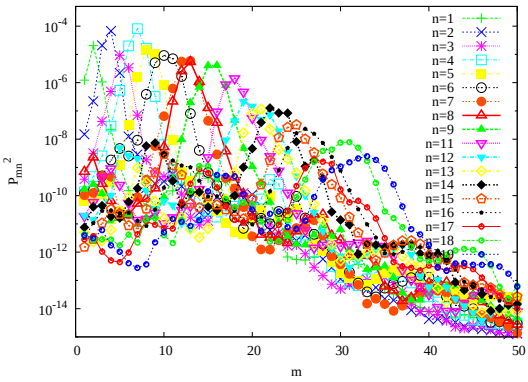

FIG. 4: Fourier amplitudes of the pressure for positive $m < 50$ and $n < 20$. A sum of m and $-m$ is taken.

The broad-band property is more clearly observed in the pressure power spectra P^2_{mn} in Fig.4. The spectra are plotted for $m \leq 50$, $n < 20$ at $t = 60$. The peaks of the power spectra for low ns consist of relatively small numbers of poloidal wavenumbers and the bandwidths of the peaks are narrow. However, the bandwidths of the peaks in the wavenumber-space become broader for larger ns. Some spectra such as $n = 18$ and 19 have multiple peaks. The shorter peaks are considered as parts of linear eigen-modes with different ns. Because of the broad-band property of the eigen-functions, we identify that the time evolution in this simulation is governed by the ballooning instability.

The time evolutions of the pressure structures are observed more closely. In Fig.5(a)-(c), the contours of the pressure fluctuations on a vertically-elongated poloidal cross-section are drawn at (a)$t = 60$, (b)70 and (c)120, respectively. In Fig.5(a), pressure fluctuations are observed in a relatively narrow area, with $m = 12 \simeq 15$ structures. The appearance of the detailed structures are different among many poloidal cross-sections, depending on the phases and amplitudes of the Fourier coefficients of the pressure fluctuation, and some other structures are observed in a different poloidal cross-section. Nevertheless, the pressure fluctuations are localized in the outer side of the torus (the right-hand-side of the figures) on the all poloidal cross-sections, being independent to the detailed structures. It also represents clearly that the evolutions of the fluctuations are governed by the ballooning instability. In Fig.5(b)($t = 70$), the area covered by the contours grows broader. In Fig.5(c)($t = 100$), the fluctuations become extremely large and cover almost the all finite-β area. The $m \simeq 2$ structures in the figure may be related to the dominance of $m/n = 2/1$ Fourier coefficients in Fig.2(b) and (c). In Fig.5(d) the radial profiles of the mean pressure P_{00} at some typical times are plotted. The modification of the P_{00} becomes gradually clear after $t = 60$. (See Fig.5(b) at $t = 70$, too.) A clear local flattening in P_{00} is observed at $t = 80$. There are multiple radial positions where the gradient of P_{00} becomes very small compared to other positions. The vertical arrows represent the positions of the rational surfaces of the $n = 1$, 2, 8 and 9 primary Fourier coefficients and the horizontal arrows represent their roughly-estimated half widths as typical examples of the areas of influences of the ballooning modes. Since these areas of influences overlap to each other, the local pressure-flattening does not work efficiently to suppress the growth of the ballooning modes when multiple ballooning modes of similar growth rates are excited simultaneously. In fact, in Fig.5(d), the dynamical evolution of the instability continues even after the local flattening is observed at $t = 80$. At $t = 90$, the pressure gradient is lost from the central part and becomes opposite to the initial gradient at the saturation time $t = 120$.

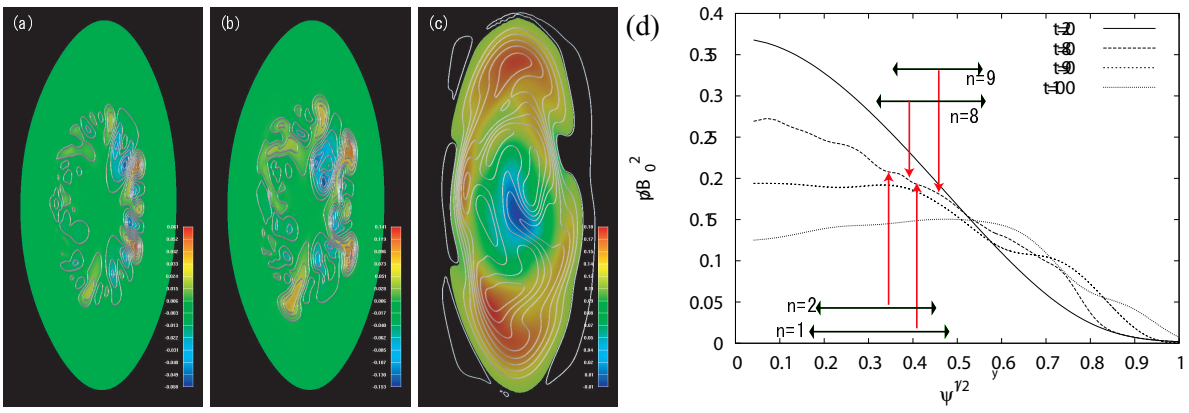

FIG. 5: The contours of the pressure fluctuations on a vertically-elongated poloidal cross-section at (a)$t = 40$, (b)70 and (c)120. (d)The radial profiles of P_{00} at $t = 20$, 80,90 and 120.

4 Milder saturation by the parallel heat conduction

In the near-ideal simulation in the above, the pressure profile is totally modified. On the other hand, we do not observe such a serious crash in a real experiment at such a low-β ($\langle\beta\rangle \simeq 1.2\%$), and achieve a high-$\beta$ value.[2, 3, 4] One important difference between the experiments and the near-ideal simulation in the above can be found in the parallel heat conduction. Although the parallel heat conduction is neglected in the ideal MHD analysis and small in the *near-ideal* simulations,

the parallel heat conduction should be large in real hot plasmas. Since the parallel heat conduction suppresses the growth of the pressure fluctuations, it can play significant roles for the study of the ballooning instability in helical plasmas. In fact, it has been shown by our earlier simulations with relatively large viscosities[6, 7] that the introduction of the parallel heat conductivity contributes to suppress the growth of unstable modes and the plasma can move to a quasi-steady state with the parallel flow. Here we carry out a simulation with the parallel heat conductivity, keeping the viscosity being much lower than the values in the earlier works.

In Fig.6, typical results of the simulation with the parallel heat conduction $\kappa_{\parallel} = 1 \times 10^{-2}$. Fig.6(a) is the isosurfaces of the pressure at the saturated time of the simulation and (b) is the mean pressure profile P_{00}. Although the mean pressure profile is strongly modified by the evolution of the ballooning instability, the modification processes are saturated at $t = 120$ and the pressure gradient is almost flat, not opposite to the initial pressure gradient as that in the near-ideal simulation shown in Fig.5(d). Since the parallel heat conductivity should be much larger in the real experiments (typically $\kappa_{\parallel}/\kappa_{\perp} > 10^{10}$), the stabilizing effect of the parallel heat conduction is also expected being much greater than that in this simulation. Thus the numerical results of the near-ideal simulation in the previous section does not imply a possible crash of the helical plasma but indicates that the mechanisms which originate from an ideal MHD system, the pressure flattening and the parallel energy release, are insufficient to suppress the ballooning instability in the helical system and some other mechanisms are required for the hot plasma to survive it. The parallel heat conduction can work to suppress when the coefficient is sufficiently large.

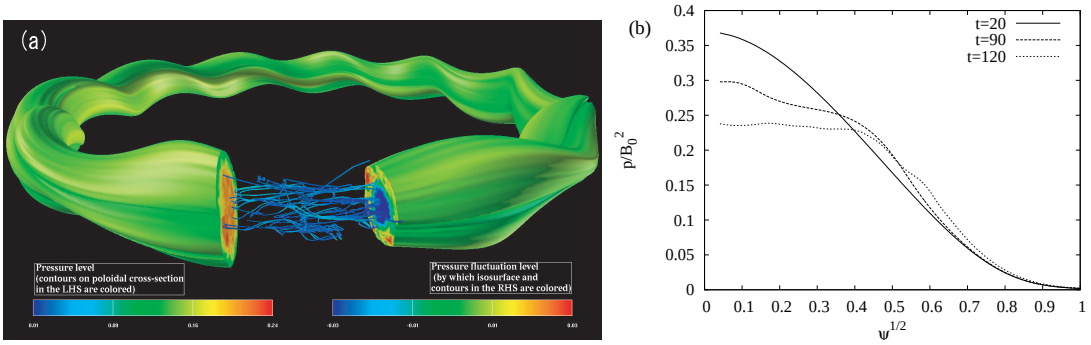

FIG. 6: Numerical results by the $\kappa_{\parallel} = 1 \times 10^{-2}$ simulation. (a)The isosurface of the pressure. Contours of the pressure and pressure fluctuations are shown in the poloidal cross-sections in the left-hand-side and the right-hand-side, respectively. (b)The mean pressure profile P_{00}

5 Concluding Remarks

We have carried out near-ideal MHD simulations and studied the growths and saturations of high-wavenumber unstable ballooning modes. Evolutions of the high-n ballooning modes are identified clearly. The growth of the high modes bring about local flattening at several radial positions. The free energy to drive the instability is much more released in the parallel direction than in the perpendicular direction and weaken the impact of the ballooning instability. Although these two mechanisms are reported to suppress the instability successfully when the unstable modes are limited to relatively low ns, they are found being insufficient when high-n ballooning modes grow simulatenously with the similar growth rates. In such helical plasmas, it appears difficult to satisfy the implicit expectation of the high modes being harmless in the frame work of ideal-

MHD mechanisms and the suppression of the high-*n* ballooning modes should be expected to some mechanisms other than the ideal MHD. One good candidate of such additional stabilization mechanisms is found in the parallel heat conduction, which has been shown to work well in this article.

Numerical simulations in this article are carried out in the NEC SX-7 “plasma simulator” and SX-8 “LHD numerical analyses system” of the National Institute for Fusion Science (NIFS), Japan. The authors would like to thank to Prof. Todo and the other members of the LHD and Magnetic Confinement Simulation Project in NIFS. for fruitful discussions.

References

[1] MOTOJIMA, O., et al., “Initial physics achievements of large helical device experiments”, Phys. Plasmas **6** (1999) 1843-1850.

[2] MOTOJIMA, O., et al., “Overview of confinement and MHD stability in the Large Helical Device”, Nuclear Fusion **45** (2005) S255-S265.

[3] SAKAKIBARA, S., et al., “MHD characteristics in the high beta regime of the Large Helical Device”, Nuclear Fusion **41** (2001) 1177-1183.

[4] WATANABE, K., et. al., “Effects of global MHD instability on operational high beta-regime in LHD ”, Nucl. Fusion **45** (2005) 1247-1254.

[5] MIURA, H., et al., “Non-disruptive MHD Dynamics in Inward-shifted LHD Configurations”, 20th IAEA Fusion Energy Conference (2004), IAEA-CSP-25/CD/TH/2-3.

[6] MIURA, H. et al., “Direct Numerical Simulation of Nonlinear Evolution of MHD Instability in LHD”, AIP Conference Proceedings **871** (2006) pp.157-168.

[7] MIURA, H. et al., “Nonlinear Evolution of MHD Instability in LHD”, Fusion Science and Technology **51** (2007) pp.8-19.

[8] MIURA, H., et al., “Nonlinear MHD Simulations in the Large Helical Device”, Phys. Plasmas **8** (2001) 4870.

[9] ICHIGUCHI, K., et al., “Nonlinear MHD analysis for LHD plasmas”, Nuclear Fusion **43** (2003) 1101-1109.

[10] NAKAJIMA, N., et al., “Growth Rates and Structures of MHD Modes in Stellarator/Heliotron”, J. Plasma Fusion and Res. SER. **6** Vol.6 (2004) 45-50.

[11] LELE, S. K., “Compact Finite Difference Schemes with Spectral-like Resolution”, J. Compu. Phys. **103** (1992) 16-42.

[12] HARAFUJI, H., et al., “Computational Study of Three-Dimensional Magnetohydrodynamic Equilibria in Toroidal Helical Systems”, J. Comp. Phys., **81** (1989) 169.

[13] NÜHRENBERG, C., “Compressional ideal magnetohydrodynamics: unstable global modes, stable spectra, and Alfvén eigen-modes in Wendelstein 7-X-type equilibria”, Phys. Plasmas, **6** (1999) 137.